RSC Advances

PAPER

View Article Online
View Journal | View Issue

Cite this: *RSC Adv.*, 2015, **5**, 42506

Novel hybrid chitosan blended MoO_3–TiO_2 nanocomposite film: evaluation of its solar light photocatalytic and antibacterial activities

P. Magesan, S. Sanuja and M. J. Umapathy*

Received 31st March 2015
Accepted 28th April 2015

DOI: 10.1039/c5ra05692f

www.rsc.org/advances

In the present study, we report newly synthesized TiO_2 and MoO_3–TiO_2 nanocomposites and chitosan and chitosan-blended MoO_3–TiO_2 nanocomposite films by sol–gel and solution cast methods, respectively. The synthesized nanocomposite films were characterized by XRD, FT-IR, TG-DTA and FESEM with EDAX. The antibacterial activities of the prepared nanocomposite films were tested against *E. coli* using the well diffusion method. The photocatalytic activities of the materials were investigated against methyl orange dye as a model organic pollutant under the irradiation of solar light. Furthermore, the mechanical properties (tensile strength and elongation) were determined using a Universal Testing Machine. From the obtained results, it was concluded that the chitosan-blended MoO_3–TiO_2 nanocomposite film exhibited higher photocatalytic, antibacterial and mechanical properties than the other materials.

1. Introduction

Recently, the ecological glitches associated to the pollution of water sources have attracted a considerable attention. One of the main sources for the contamination of water pollution are the textile industries that consume large quantities of water and produce large volumes of waste water from different steps in the dyeing and finishing process. The worldwide dye consumption by dyeing industries is around 10^7 kg per year.[1] Because the dyes are stable, recalcitrant, colorant and even potentially carcinogenic and toxic, their release into the environment causes a major threat to the environment.[2] The dye contaminated waste water cannot be easily treated because the natural biodegradability has become an increasingly difficult task due to the improved properties of dyestuffs. A wide range of conventional methodologies have been used to eliminate these pollutants from the waste water but their efficiency is limited. Modern nanotechnologies have become popular for the fabrication of desirable nanomaterials with large surface-to-volume ratios of unique surface properties for treating these pollutants. Nanoparticles are key to nanotechnology; therefore, the in-depth study of nanomaterials is an important source for producing new principles, techniques and methods.[3] From an environmental standpoint, heterogeneous photocatalysis is an important pioneering technology for applications in water purification. With the advent of nanotechnology, semiconductor nanoparticles have attracted considerable attention due to their novel optical, electrical and mechanical properties. Among the various semiconductor nanoparticles, nanosized titanium dioxide (TiO_2) particles are the most frequently studied one in the field of solar energy conversion, photocatalysis, transparent UV protection films and chemical sensors. It has been proven to be one of the most suitable materials for environmental remediation processes due to its powerful oxidation strength, low cost, non-toxicity and chemical stability against photo-corrosion.[4–6] However, in practical applications, the conventional TiO_2 photocatalyst has certain disadvantages such as the effective utilization of UV/solar light and a large surface area requirement for the adsorption of pollutant, that is, the adverse recombination of electron and holes. Many efforts have been made to extend the adsorption of light from the UV to the visible region and to improve the photocatalytic efficiency of TiO_2.[7] Enhancing the rate of photoreduction by doping a semiconductor with metal ions can produce a photocatalyst with an improved trapping-to-recombination rate ratio. However, when metal ions or oxides are incorporated into TiO_2 by doping, the impurity energy levels formed in the band gap of TiO_2 can also lead to an increase in the rate of recombination between photogenerated electrons and holes. Photocatalytic reactions can occur only if the trapped electron and hole are transferred to the surface of the photocatalyst. This means that metal ions should be doped near the surface of the photocatalyst to allow the efficient charge transfer. Dopants such as transition metals (Fe, Al, Ni, Cr, Co, W, V and Zr) and metal oxides (Fe_2O_3, Cr_2O_3, CoO_2, and SiO_2) have been used to improve the applicability of photocatalysts.[8–10] The absorption threshold of TiO_2 nanopowder has been shifted from the UV to the visible region by doping with visible light active material and photocatalytic efficiencies higher than the pure TiO_2 and Degussa P25 have been obtained.[11–14] As a wide-band gap n-type semiconductor, molybdenum oxide (MoO_3) is

---

Department of Chemistry, College of Engineering Guindy Campus, Anna University, Chennai-25, India. E-mail: mj_umapathy@yahoo.co.in; Tel: +91-44-22358669

a potential material because of its wide range of stoichiometry and interesting behavior which includes its chemical,[15] structural,[16] electrical and optical[17] properties. Surface modification with MoO_3 causes TiO_2 nanoparticles to become much more hydrophilic and they can be more stably suspended in an aqueous solution. It is believed that the source of the excellent dispersibility in an aqueous solution originates from the high hydrophilicity of MoO_3.[18] The addition of MoO_3 to TiO_2 showed high activity for the photodegradation of molasses. The MoO_3–TiO_2 material has a larger surface area compared to the pure oxides. The modified material has a reduced band gap and can absorb more light in the near-visible region, and thus accelerate the rate of decomposition.[19]

Over the recent years, hybrid materials based on chitosan have been developed, including conducting polymers, metal nanoparticles and oxide agents, due to the excellent properties of the individual components and outstanding synergistic effects.[20] In this regard, chitosan, a linear cationic, pH sensitive, non-toxic, biodegradable and biocompatible polysaccharide prepared from the deacetylation of chitin appears to offer numerous distinct advantages.[21] It is the second most abundant biopolymer that is widely present as the basic components of the exoskeletons of crustaceans and insects. The structure of chitosan is similar to that of cellulose; it consists of a β-(1–4)-linked D-glucosamine residue with 2-hydroxyl group being substituted by an amino or acetylated amino group. The structures of cellulose, chitin and chitosan are shown in Fig. 1. Chitosan is soluble in diverse acids and can interact with polyanions to form complexes and gels. It has the adsorption capacity of 1000–1100 g kg^{-1}, which is higher than that of activated carbon; thus, it is a super high-capacity adsorbent for the removal of contaminant from water.[22] This high adsorption capacity of chitosan gives rise to the binding ability of chitosan with contaminants in water through the hydroxyl and amino groups present on the surface. Currently, researchers have been devoted to fabricate the combination of chitosan and metal oxide nanomaterials for environmental remediation. The objective of this study is focused on (i) synthesis and characterization of TiO_2 and MoO_3–TiO_2 nanocomposites and chitosan and chitosan-blended MoO_3–TiO_2 nanocomposite films by sol–gel and solution cast methods, (ii) photocatalytic activities of the prepared nanocomposites and films towards the degradation of methyl orange dye under the illumination of solar light, (iii) antimicrobial activity of the nanocomposite films against *E. coli* using the well diffusion method, and (iv) the mechanical properties (tensile strength and elongation), which were determined using a Universal Testing Machine.

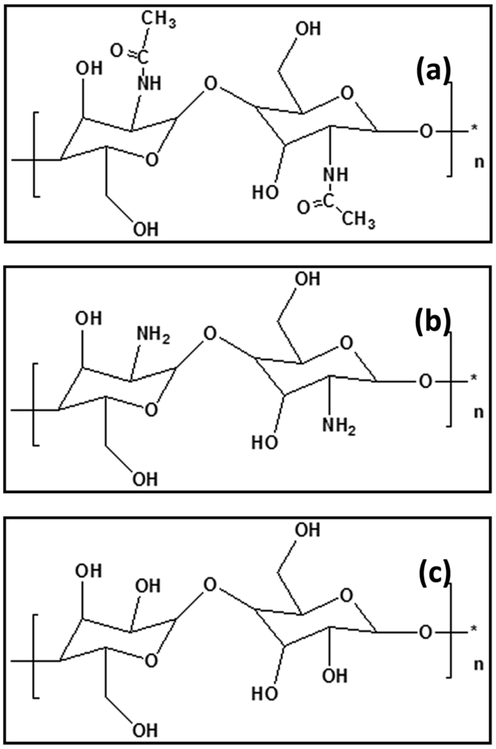

Fig. 1 Comparison of (a) chitin (b) chitosan and (c) cellulose formulae.

2. Experimental details

2.1. Materials

Titanium tetraisopropoxide (TTIP) and Tween-80 were purchased from Spectrochem and molybdenum trioxide (MoO_3) was purchased from SRL. Crab shells were collected from Kasimedu Seafood Market and sodium hydroxide and hydrochloric acid were purchased from Merck. Glacial acetic acid was obtained from Qualigens and used as received. Freshly prepared de-ionized water was used in all the experiments.

2.2. Synthesis of MoO_3–TiO_2 and TiO_2 nanocomposites

MoO_3 nanoparticles were suspended in 20 mL of distilled ethanol and stirred for 30 minutes. To the homogeneous dispersion, 3 mL of Tween-80 was added with stirring, and it was further stirred for 30 minutes. A mixture of 3 mL TTIP with 10 mL isopropyl alcohol was added drop wise into the suspension and the stirring was continued for 2 h to obtain a gel. The resultant gel was filtered-off and washed thoroughly with 1 : 1 aqueous ethanol, filtered and then oven dried at 120 °C for 6 h. The solid sample was calcined at 500 °C for 3 h using an electrical muffle furnace. The similar procedure was followed for the preparation of TiO_2 nanocomposites without adding MoO_3 nanoparticles.

2.3. Synthesis of chitosan from crab shell

The crab shells were collected from Kasimedu Seafood Market, Chennai, Tamil Nadu, India. The crabs exoskeletons collected were placed in Ziploc bags and refrigerated overnight. The synthesis of chitosan was performed by performing the following four steps:

(i) Coarse purification. Approximately 500 g of crab shells were coarsely cleaned with running water until sand and other impurities such as soils were removed. The cleaned crab shells were dried overnight in a hot air oven at 110 °C.

(ii) Deproteinization. The dried shell samples were ground using a mortar and transferred to a beaker. 2% of NaOH was added to the beaker containing the shell samples and heated with stirring at 60–70 °C for 30 minutes. The shell samples were filtered off with a strainer and the process was repeated a few more times until the filtrate became clear and colorless. The samples were washed with demineralized water to remove the unreacted NaOH. For saving time, the shell samples can be soaked in NaOH solution overnight after the first NaOH treatment, followed by filtering and washing.

(iii) Demineralization. 7% HCl was slowly added to the shells and the mixture was stirred at room temperature until effervescence ceased. The mixture was filtered-off and washed with excess distilled water. The samples were dried overnight in a hot air oven at 60 °C to obtain around 100 g of chitin. This step is known as demineralization.

(iv) Synthesis of chitosan from chitin by partial deacetylation. Chitin was loaded in a RB flask with 50% NaOH. The samples were heated at 125 °C for 2 h and then allowed to cool down followed by the addition of 250 mL of water. On the next day, the sample was filtered-off and the residue was washed with excess water and dried in a hot air oven at 60 °C for 2 h.

2.4. Casting of the chitosan film

A chitosan film was synthesized by a solution cast method. 1 g of chitosan was dissolved in 100 mL of 1% (v/v) acetic acid solution and stirred for 24 hours. Subsequently, it was sonicated for 15 min for efficient dispersion. It was then cast into a Petri-dish and placed in an oven at 50–60 °C for overnight to obtain a homogeneous film.

2.5. Casting of chitosan-blended MoO_3–TiO_2 nanocomposite film

1 g of prepared MoO_3–TiO_2 composites was added into the chitosan solution (1 g of chitosan in 100 mL of 1% (v/v) acetic acid) and the mixture was sonicated for 30 minutes and stirred continuously for 12 h until a clear solution was obtained. The solution was cast onto Petri plates and dried at room temperature for 48 h to obtain the composite film.

2.6. Solar light intensity measurements

Solar light intensity was measured every 30 min and the average light intensity over the period of each experiment was calculated. The sensor was always set in the position of maximum intensity. The intensity of solar light was measured using a New 200 000 Lux Digital Meter Light Luxmeter Meter Photometer with a Footcandle FC. The intensity was $1200 \times 100 \pm 100$ lux and it was nearly constant throughout the course of the experiments.

2.7. Photocatalytic degradation of methyl orange dye

The photocatalytic experiments were carried out under identical conditions on sunny days between 11 a.m. and 2 p.m. In all the experiments, 50 mL of the reaction mixture was irradiated under sunlight. An open borosilicate glass tube of 50 mL capacity, 40 cm height and 20 mm diameter was used as the reaction vessel. The suspensions were magnetically stirred in the dark for 15 min to obtain an adsorption–desorption equilibrium between the dyes and TiO_2 and MoO_3–TiO_2 nanocomposites and chitosan and chitosan-blended MoO_3–TiO_2 nanocomposite films. Irradiation was carried out under open-air conditions. 50 mL of the dye solution with the synthesized catalysts were constantly aired by a pump to provide oxygen and for the thorough mixing of the reaction solution. It was observed that the solvent did not volatilize during the illumination time. After dark adsorption, the first sample was analyzed. At specific time intervals (15 min), 2–3 mL of the sample was withdrawn and centrifuged to separate the catalyst. 1 mL of the sample was properly diluted and its absorbance at 464 nm was measured immediately to monitor the degradation of the methyl orange.

2.8. Determination of antibacterial activity

The *in vitro* antibacterial action of the prepared samples was examined using Gram negative bacteria (*Escherichia coli* ATCC 25922) by the well diffusion method. Nutrient agar was prepared and poured into sterile Petri dishes and allowed to solidify. Bacterial cultures (*E. coli*) grown for 24 h were swabbed on it. 5 wells (10 mm diameter) were made using a cork borer. Four different concentrations (250 μg, 500 μg, 750 μg and 1000 μg) of the nanoparticle and one negative control were loaded into the wells. The plates were then incubated at 37 °C for 24 h. After incubation, the inhibition diameter was measured. The percentage of inhibition was calculated using the following formula (eqn (1))

$$\% \text{ of inhibition} = \left\{\frac{I(\text{diameter of the inhibited zone})}{90(\text{diameter of the Petri-plate in mm})} \times 100\right\} \quad (1)$$

2.9. Instrumentation and analysis

The following physiochemical techniques have been used to characterize the prepared catalysts. To characterize the phase structure of the TiO_2 and MoO_3–TiO_2 nanocomposites and chitosan and chitosan-blended MoO_3–TiO_2 nanocomposite films, a Bruker D2 Phaser Desktop X-ray Diffractometer equipped with Ni-filtered Cu Kα radiation ($\lambda = 1.542$ Å) was used, and it was operated at an accelerating voltage and emission current of 30 kV and 10 mA, respectively. Data were acquired over the range of 2θ from 0° to 70 ° with a step size of 0.0017 and a scan rate of 7° min^{-1}. Field emission scanning electron microscopy (FESEM) was performed to examine the surface morphology of the prepared nanocomposites using a DXS-10 ACKT scanning electron microscope equipped with EXS, which was used to study the elemental composition. For Fourier transform infrared spectroscopy (FT-IR) analysis, the KBr pellets were prepared from the TiO_2 and MoO_3–TiO_2 nanocomposites and the chitosan and chitosan-blended MoO_3–TiO_2 nanocomposite films. FT-IR analysis was performed using a spectrophotometer (Perkin Elmer RX1 instrument). Thermogravimetric-differential thermal analysis (TG-DTA) of the nanocomposites was carried out on a WATERS SDT Q 600 TA model instrument. Mechanical properties (tensile strength and elongation) of the films were determined according to the ASTM standard method with a Universal Testing Machine (TNUM-5900). The film was cut into (7 × 3 cm) rectangular shapes before measurements.

3. Results and discussion

3.1. Surface morphology of TiO_2 and MoO_3–TiO_2 nanocomposites and chitosan and chitosan-blended MoO_3–TiO_2 nanocomposite films

Field emission scanning electron microscopy (FESEM) was used to investigate the surface morphology of the prepared chitosan film, TiO_2, MoO_3–TiO_2, and chitosan-blended MoO_3–TiO_2 composite film. The FESEM images of chitosan, TiO_2, MoO_3–TiO_2 nanocomposites and chitosan-blended MoO_3–TiO_2 nanocomposite film are shown in the Fig. 2(a)–(d), respectively. The chitosan, TiO_2, MoO_3–TiO_2 and chitosan-blended MoO_3–TiO_2 composite film had an aggregated particle structure with an almost spherical morphology. However, at the same time, TiO_2 and MoO_3–TiO_2 nanocomposites revealed the agglomeration of the nanoparticles, which may be due to the presence of the templating agent. As can be seen in the Fig. 2(d), it is worth noting that the chitosan particles were non-uniformly mixed in the MoO_3–TiO_2 matrix.

3.2. Elemental composition

The elemental compositions of the TiO_2 and MoO_3–TiO_2 nanocomposites and chitosan-blended MoO_3–TiO_2 nanocomposite film were studied by energy dispersive X-ray analysis (EDAX). Fig. 3(a)–(c) depicts the EDAX analysis of the TiO_2, MoO_3–TiO_2 and chitosan-blended MoO_3–TiO_2 composite film, respectively, from a selected area in the binding region of 0–10 keV. The signals from the spectra reveal the presence of Ti, O, Mo and C in the prepared nanocomposites. This result corroborates the formation of the chitosan–MoO_3–TiO_2 nanocomposite film.

3.3. Crystalline phases

The crystalline phases of the prepared TiO_2 and MoO_3–TiO_2 nanocomposites and chitosan and chitosan-blended MoO_3–TiO_2 nanocomposite films were studied by X-ray diffraction analysis. Fig. 4 depicts the XRD pattern of the prepared nanocomposites. In TiO_2, MoO_3–TiO_2 and chitosan-blended MoO_3–TiO_2 composite film, TiO_2 exists in the anatase phase, showing sharp characteristic peaks at $2\theta = 25.3°$, 37.8°, 48.1°, 54.0°, 55.1°, 62.8° and 75.0° corresponding to the (101), (004), (200), (105), (211), (204) and (215) planes, respectively, which agree well with the standard JCPDS card no. 89-4921, and thus confirm that the nanocomposite are predominantly crystalline in nature with an anatase phase. The characteristic peaks of MoO_3 were not observed, and thus it can be inferred that the doping of MoO_3 did not influence the crystal structure of the TiO_2 particles. It is clear that the chitosan is highly crystalline in nature and shows the characteristics peaks at $2\theta = 9.2°$, 19.2°, 26.9°, 34.9°, 38.8°, 43.5°, 51.0° and 72.8°, which suggests the formation of inter- and intra-molecular hydrogen bonds in the presence of free amino groups in the chitosan. The average crystallite sizes of the nanocomposites have been deduced from the half-width of the full maximum (HWFM) of the most intense peak using the Scherrer equation (eqn (2)) as follows:

$$t = K\lambda/\beta \cos\theta, \quad (2)$$

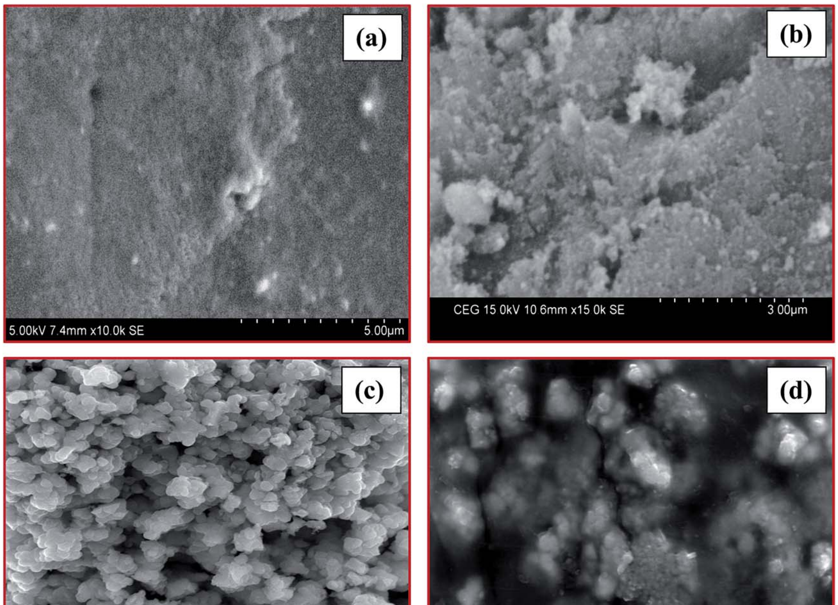

Fig. 2 FESEM micrographs of (a) chitosan film, (b) TiO_2, (c) MoO_3–TiO_2 and (d) chitosan-blended MoO_3–TiO_2 film.

where t is the crystallite size, K is the shape factor with a value of 0.9, λ is the wavelength of the X-ray used. θ is the Bragg diffraction angle, β is the corrected line broadening and $\beta = \beta_b - \beta_s$, β_b is the broadened profile width of the experimental sample and β_s is the standard profile width of the reference (high purity silica) sample. According to eqn (2), the average crystallite sizes of the prepared samples are listed in Table 1.

3.4. Fourier transform infrared spectroscopy (FTIR)

FTIR spectrum provides information on the nature of the synthesized nanocomposites. The FTIR spectra of the TiO_2 and MoO_3–TiO_2 nanocomposites, chitosan and chitosan-blended MoO_3–TiO_2 nanocomposite film are presented in Fig. 5. The spectra of chitosan and chitosan-blended MoO_3–TiO_2 composite film (Fig. 5(c) and (d)) show absorption peak at 3423–3500 cm^{-1} and 1643–1647 cm^{-1}, which are attributed to the amine ($-NH_2$) and hydroxyl (–OH) functional groups, respectively.[23] Both these functional groups on the chitosan chain can serve as coordination and reaction sites for the adsorption of organic species.[24] Fig. 5(a), (b) and (d) also confirms the existence of metal oxide (TiO_2) peak around 742–783 cm^{-1} for TiO_2, MoO_3–TiO_2 and chitosan-blended MoO_3–TiO_2 composite film. A weak band at around 2340–2370 cm^{-1} may be attributed to the vibrations of atmospheric CO_2. The apparent existence of amine or amide and hydroxyl functional groups together with

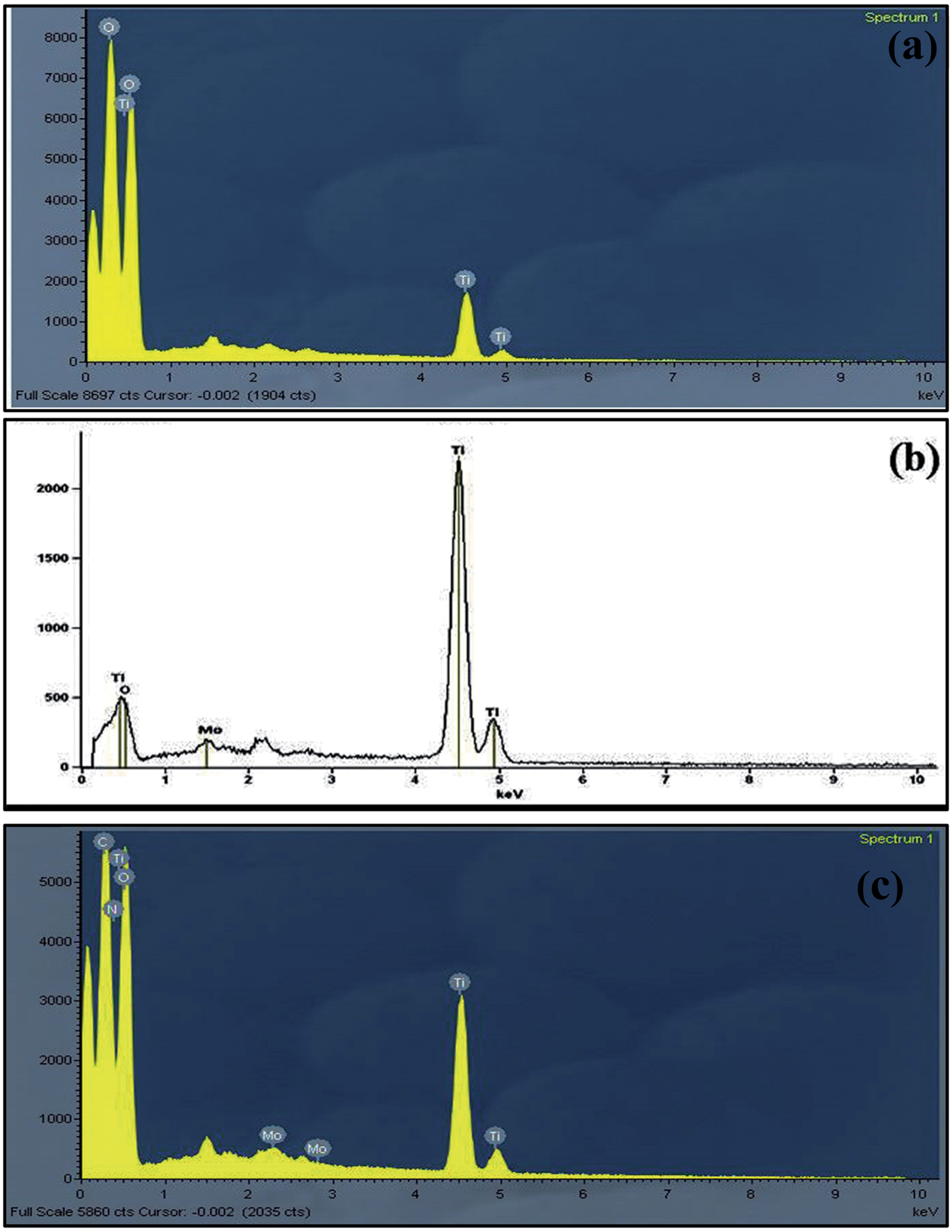

Fig. 3 EDX spectra of (a) TiO_2, (b) MoO_3–TiO_2 and (c) chitosan-blended MoO_3–TiO_2.

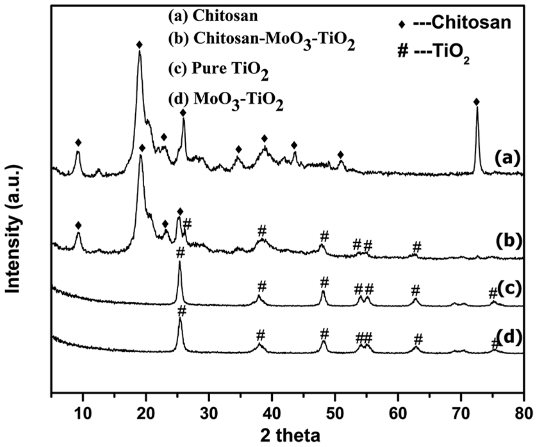

Fig. 4 XRD patterns of (a) chitosan film, (b) chitosan-blended MoO_3–TiO_2 film, (c) TiO_2 and (d) MoO_3–TiO_2.

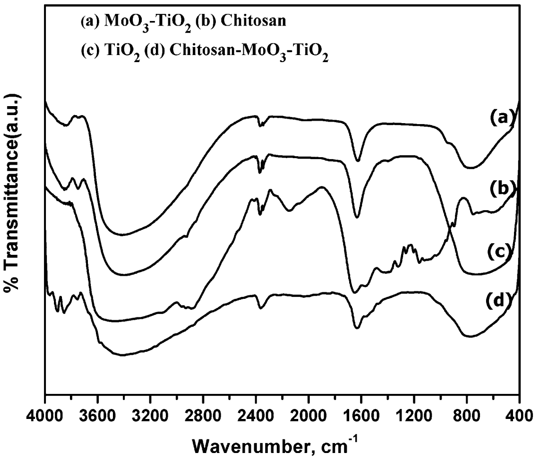

Fig. 5 FTIR spectra of (a) MoO_3–TiO_2, (b) chitosan film, (c) TiO_2 and (d) chitosan-blended MoO_3–TiO_2 film.

metal oxides should help to confirm the effective removal of the organic dyes through a photodegradation–adsorption process.[25]

3.5. TG-DTA analysis

TG-DTA analysis was carried out to study the thermal decomposition behavior of the synthesized TiO_2 and MoO_3–TiO_2 nanocomposites, chitosan and chitosan-blended MoO_3–TiO_2 nanocomposite film, and are shown in Fig. 6. The synthesized chitosan film shows two weight loss curves, first stage of weight loss was due to the evaporation of water and the second stage of weight loss was due to the degradation of the polymer chains. In the TGA of TiO_2, three noticeable steps were observed, which were in the range of 200–340 °C, 341–400 °C and 500–585 °C. The TGA curve shows two exothermic peaks: the first sharp and narrow exothermic peak with a maximum of 282 °C may be attributed to the burnout of the templating agent and the second weak exothermic peak corresponds to the crystallization process of TiO_2 with a maximum of 354 °C.[26] In the TG-DTA curve of MoO_3–TiO_2, two main exothermic peaks were found: a larger peak centered around 363 °C and a sharp peak centered around 401 °C. This may be attributed to the burnout of the surfactant template and crystallization process, respectively. In the chitosan-blended MoO_3–TiO_2 film, three weight losses were observed. At 100 °C, the first weight loss was observed, which was due to the evaporation of water; the second weight loss around 150 °C was due to polymer degradation and the last and final weight loss at 400 °C was due to the decomposition of organic matter and then the compound remained intact.

3.6. Photocatalytic activity

For the efficient use of solar light or the visible region of the spectrum, the technologies that expand the absorption scope of TiO_2 provide an attractive challenge for developing the future generation of photocatalysts.[27] The visible light photocatalytic activity of the F-doped TiO_2 was achieved by creating oxygen vacancies.[28] Bismuth oxohalide nanoplates on TiO_2 nanoribbons act as sunlight-driven bifunctional photocatalysts for all-weather removal of pollutants. The BiOBr@TiO_2 framework exhibits a very impressive sunlight-driven photocatalytic activity, which is much higher than that exhibited by commercially available P25 TiO_2 under the same conditions.[29] The photocatalytic activity of the TiO_2 and MoO_3–TiO_2 nanocomposites and chitosan and chitosan-blended MoO_3–TiO_2 nanocomposite films was investigated by the photodegradation of the methyl orange dye (model organic pollutant) over a period of 2 h under solar light irradiation. Percentage removal was calculated using eqn (3).

Table 1 Average crystallite size (*T*) obtained from the XRD analysis and zone of inhibition of TiO_2 and MoO_3–TiO_2 nanocomposites and chitosan and chitosan-blended MoO_3–TiO_2 nanocomposite films against *E. coli*[a]

			Zone of inhibition, mm			
S. no.	Nanocomposites	*T*, nm	250 μg	500 μg	750 μg	1000 μg
1	TiO_2	12	NA	NA	NA	NA
2	MoO_3–TiO_2	11	NA	NA	9	11
3	Chitosan film	16	NA	9	10	11
4	Chitosan-blended MoO_3–TiO_2 film	17	NA	10	12	13

[a] NA – non-active.

$$\%\ \text{removal of model pollutant} = \frac{C_o - C_t}{C_o} \times 100 \tag{3}$$

where C_o is the concentration of model pollutant at 0 min and C_t is the concentration of model pollutant at experimental time t.

The photocatalytic mechanism was as follows: when the synthesized nanoparticles were illuminated under solar light irradiation, the electron transition from the valence band (VB) to the conduction band (CB) resulted in the electron (e^-)–hole (h^+) pair, in which the electron (e^-) was reductive, while the hole (h^+) was oxidative. The general photocatalytic mechanism is shown in Fig. 7. The hole (h^+) reacted with OH^- on the surface of the nanomaterials, generating hydroxyl radicals ($^{\bullet}OH$), superoxide anion (O_2^-) and perhydroxyl radicals (HO_2^-). $^{\bullet}OH$ radicals are extraordinarily reactive species and attack most of the organic molecules with rate constants usually in the order of 10^6–10^9 M^{-1} s^{-1}. Fig. 8 displays the photodegradation profiles of methyl orange dye by the synthesized nanocomposites. It can be seen from the Fig. 8, that all the samples were capable of degrading methyl orange, as indicated by the decrease in the methyl orange solution concentration throughout the period of the photocatalytic study; however, the TiO_2 did not exhibit any photocatalytic activity under the identical conditions. Besides, the photocatalytic activity increased in the order TiO_2 < MoO_3–TiO_2 < chitosan film < chitosan-blended MoO_3–TiO_2 composite film. Therefore, chitosan-blended MoO_3–TiO_2 exhibited the highest photocatalytic activity among the investigated catalysts in the photodegradation of methyl orange. Generally, the photocatalytic activity of the catalyst is influenced by various factors, particularly by light harvesting, charge separation efficacy and the adsorption ability for target pollutants. Thus, the higher photocatalytic activity of the chitosan-blended MoO_3–TiO_2 composite film compared with pure TiO_2 under solar light irradiation was attributed to the transfer and separation of photo-generated charge among the respective energy levels of the semiconductor photocatalyst. The photocatalytic studies showed that the introduction of CNTs into TiO_2 nanofiber membranes facilitated the separation of photo-generated charges, leading to an enhancement of the photocatalytic activity towards the decomposition of methylene blue (MB) in water under the illumination of solar light.[30] The recyclability

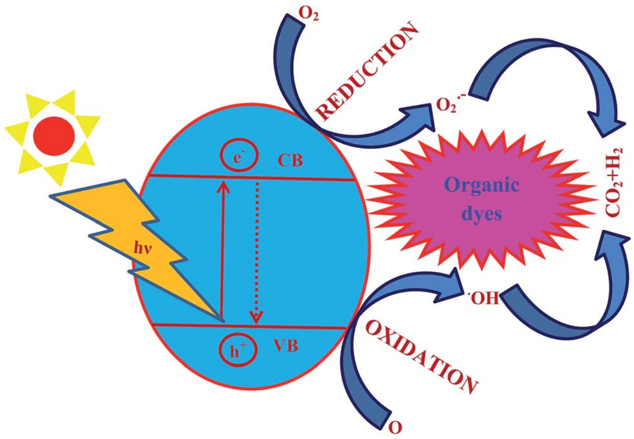

Fig. 7 General photocatalytic mechanism.

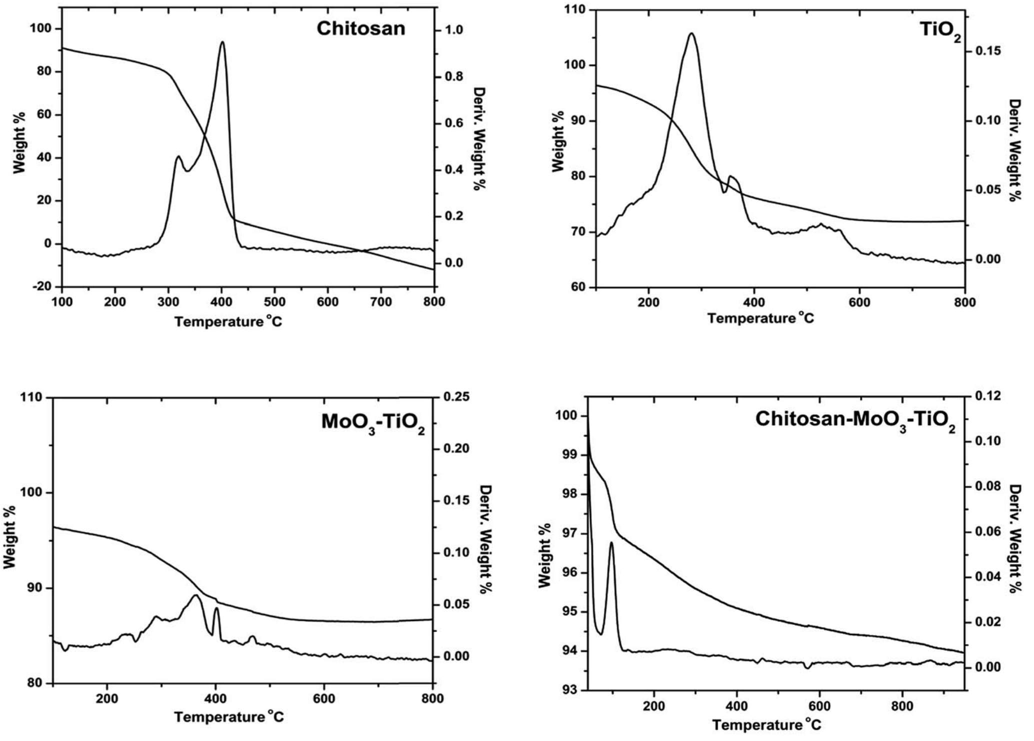

Fig. 6 TG-DTA of chitosan film, TiO_2, MoO_3–TiO_2 and chitosan-blended MoO_3–TiO_2 film.

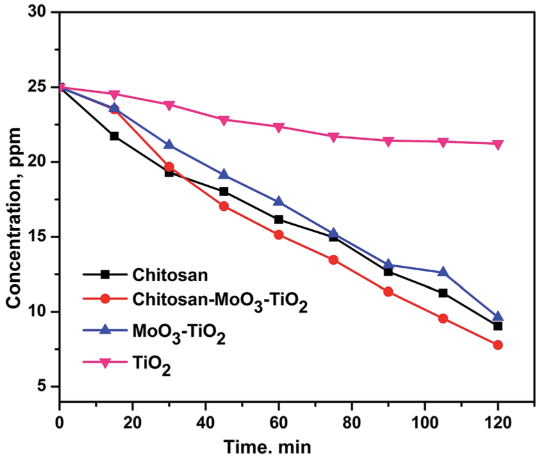

Fig. 8 Solar light photodegradation profiles of methyl orange dye.

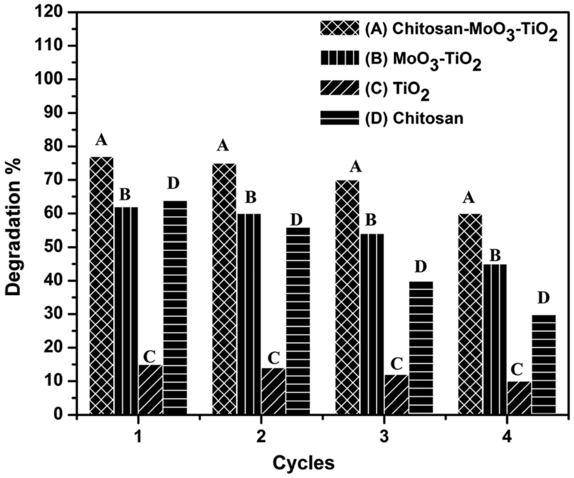

Fig. 9 Recyclability degradation percentage of the prepared composites.

experiments were performed and are shown in Fig. 9. After each experiment, the photocatalyst was washed thrice with ethanol, filtered, dried at 70 °C and reused. The catalysts showed some favorable reusability after recycling for four times. However, we did observe some extent of loss in the catalytic activity after each cycle. The decrease in the degradation rate may be due to the weakening of the absorbance ability or the loss of some catalyst during the collection of the catalysts.

3.7. Antimicrobial activity

The antimicrobial activity of synthesized chitosan-blended MoO_3–TiO_2 film (A), MoO_3–TiO_2 (B), TiO_2 (C) and chitosan film (D) were examined by the well diffusion method against the bacteria *E. coli*. The samples were tested using four different concentrations: 250 µg, 500 µg, 750 µg and 1000 µg. The zones of inhibition of the synthesized samples against *E. coli* for the various concentrations are displayed in Table 1 and the corresponding bar diagram is shown in Fig. 10. From the results of the zone of inhibition method (Fig. 11), it was observed that all the samples exhibited no activity at the concentration of 250 µg. At 500 µg, the chitosan-blended MoO_3–TiO_2 and chitosan film had 10 mm and 9 mm zones of inhibition, respectively, while MoO_3–TiO_2 and TiO_2 did not show any activity. This result can be explained by the presence of chitosan, which possessed good anti-bacterial activity. At 750 µg, the chitosan-blended MoO_3–TiO_2 film, MoO_3–TiO_2 and chitosan film showed 12, 9 and 10 mm of zones of inhibition, respectively, while TiO_2 did not show any activity even at this concentration. As we increase the concentration higher to 1000 µg, the activity increased up to 13 mm and 11 mm for the chitosan-blended MoO_3–TiO_2 film, MoO_3–TiO_2 and chitosan film, respectively; nevertheless, TiO_2 still did not show any activity. From the results obtained it was confirmed that with increasing

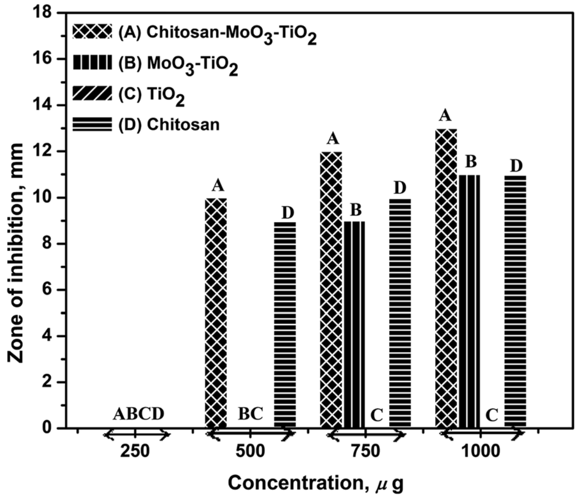

Fig. 10 Comparative study of the zone of inhibition (mm) for (A) chitosan-blended MoO_3–TiO_2 film, (B) MoO_3–TiO_2, (C) TiO_2 and (D) chitosan film in *E. coli* bacterial strain.

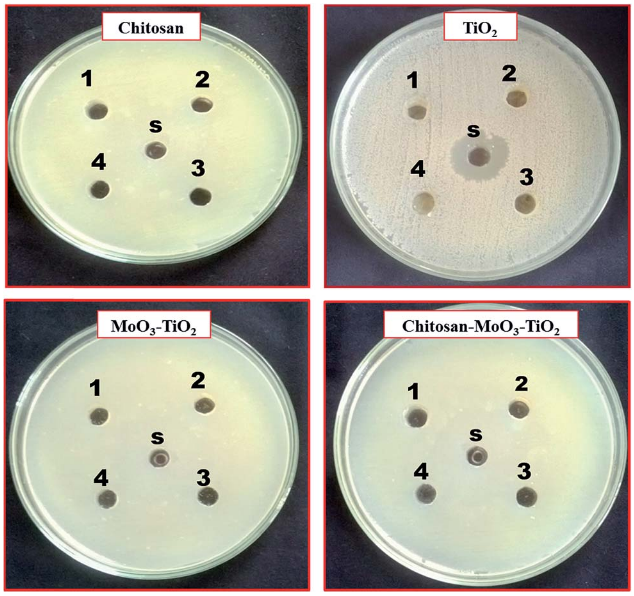

Fig. 11 Well diffusion assay of chitosan, TiO_2, MoO_3–TiO_2 and chitosan-blended MoO_3–TiO_2 nanocomposites.

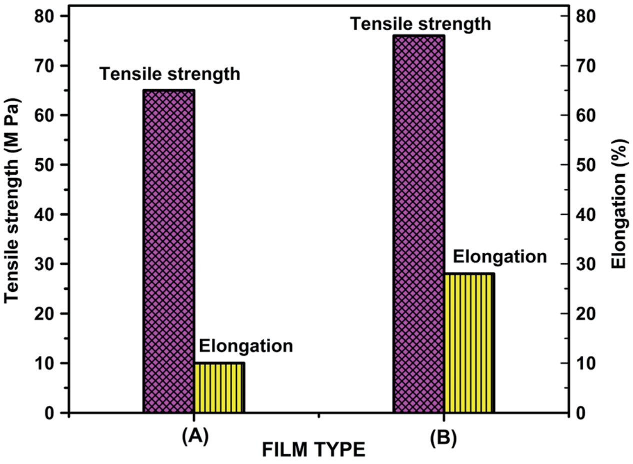

Fig. 12 Mechanical properties of (A) chitosan and (B) chitosan-blended MoO_3–TiO_2 films.

concentration of chitosan the activity increased, while TiO_2 did not show any antibacterial activity for all the four concentrations and remained inactive in the dark.

3.8. Mechanical properties

Mechanical studies of the synthesized chitosan film and chitosan-blended MoO_3–TiO_2 films were carried out, through which their tensile strength and elongation were measured and are shown in Fig. 12. The pure chitosan film exhibited a low tensile strength of 65 MPa when compared to the chitosan–MoO_3–TiO_2 film, whose strength was found to be 76 MPa. The nanoparticle doped chitosan film had a higher strength due to the strong interaction of nanoparticles and the NH_2 group present in the chitosan molecules. The elongation of the films were determined and it was observed that the chitosan film had a low elongation of 10%, while MoO_3–TiO_2 doped chitosan film had a high elongation of 28% because of the efficient dispersion of the metal oxide into the polymer film (Fig. 13).

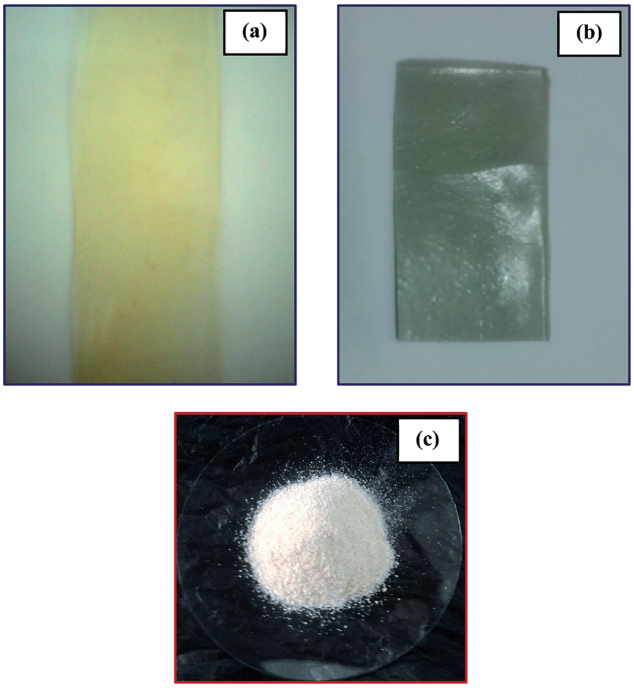

Fig. 13 Photographs of (a) chitosan film, (b) chitosan-blended MoO_3–TiO_2 film and (c) chitosan powder.

4. Conclusions

In summary, a kind of novel chitosan-blended MoO_3–TiO_2 nanocomposite film, chitosan film, MoO_3–TiO_2 and TiO_2 nanocomposites were prepared by a simple method. The synthesized materials were characterized by XRD, FT-IR, TG-DTA and FESEM with EDAX. Among the synthesized materials, the chitosan-blended MoO_3–TiO_2 nanocomposite film exhibited higher photocatalytic, antibacterial and mechanical properties. These are cost effective and environment-friendly materials for engineering applications for the removal of contaminants from water released from textile industries.

Acknowledgements

P. Magesan is thankful to the University Grants Commission, Delhi for the financial support and we thank the DST-FIST, Department of Chemistry, College of Engineering Guindy Campus, Anna University, Chennai, India for providing lab and instrument facilities for this research work.

References

1 Y. C. Wong, Y. S. Szeto, W. H. Cheung and G. McKay, *Process Biochem.*, 2004, **39**, 693.
2 G. Moussavi and M. Mahmoudi, *J. Hazard. Mater.*, 2009, **168**, 806.
3 C. Burda, X. B. Chen, R. Narayanan and M. A. El-Sayed, *Chem. Rev.*, 2005, **105**, 1025.
4 A. Nakajima, H. Obata, Y. Kameshima and K. Obata, *Catal. Commun.*, 2005, **6**, 716.
5 Q. J. Xiang, K. L. Lv and J. G. Yu, *Appl. Catal., B*, 2010, **96**, 557.
6 T. Y. Leung, C. Y. Chan, C. Hu, J. C. Yu and P. K. Wong, *Water Res.*, 2008, **42**, 4827.
7 M. A. Rauf, M. A. Meetani and S. Hisaindee, *Desalination*, 2011, **276**, 13.
8 H. K. Shon, D. L. Cho, S. H. Na, J. B. Kim, H. J. Park and J. H. Kim, *J. Ind. Eng. Chem.*, 2009, **15**, 476.
9 S. Chang and W. Liu, *Appl. Catal., B*, 2011, **101**, 333.
10 N. Venkatachalam, M. Palanichamy, B. Arabindoo and V. Murugesan, *J. Mol. Catal. A: Chem.*, 2007, **266**, 158.
11 M. S. Nahar, K. Hasegawa, S. Kagaya and S. Kuroda, *Sci. Technol. Adv. Mater.*, 2007, **8**, 286.
12 T. K. Ghorai, S. K. Biswas and P. Pramanik, *Appl. Surf. Sci.*, 2008, **254**, 7498.
13 N. D. Abazovic, L. Mirenghi, I. A. Jankovic, N. Bibic, D. V. Sojic, B. F. Abramovic and M. I. Comor, *Nanoscale Res. Lett.*, 2009, **4**, 518.

14 C. L. Luu, Q. T. Nguyen and S. T. Ho, *Adv. Nat. Sci.: Nanosci. Nanotechnol.*, 2010, **1**, 01.

15 Y. Shi, B. Guo, S. A. Corr, Q. Shi, Y. S. Hu, K. R. Heier, L. Chen, R. Seshadri and G. D. Stucky, *Nano Lett.*, 2009, **9**, 4215.

16 D. Parviz, M. Kazemeini, A. M. Rashi and K. J. Jozani, *J. Nanopart. Res.*, 2010, **12**, 1509.

17 Y. Zhao, J. Liu, Y. Zhou, Z. Zhang, Y. Xu, H. Naramoto and S. Yamamoto, *J. Phys.: Condens. Matter*, 2003, **15**, 547.

18 K. Y. Song, M. K. Park, Y. T. Kwon, H. W. Lee, W. J. Chung and W. I. Lee, *Chem. Mater.*, 2001, **13**, 2349.

19 M. Navgire, A. Yelwande, D. Tayde, B. Arbad and M. Lande, *J. Compos. Mater.*, 2012, **33**, 261.

20 L. H. Li, J. C. Deng, H. R. Deng, Z. L. Liu and L. Xin, *Carbohydr. Res.*, 2010, **345**, 994.

21 E. I. Rabea, M. E. T. Badawy, C. V. Stevens, G. Smagghe and W. Steurbaut, *Biomacromolecules*, 2003, **4**, 1457.

22 Z. Y. Liu, H. W. Bai and D. D. Sun, *New J. Chem.*, 2011, **35**, 137.

23 O. A. C. Monteiro and C. Airoldi, *J. Colloid Interface Sci.*, 1999, **212**, 212.

24 F. C. Wu, R. L. Tseng and R. S. Juang, *J. Hazard. Mater.*, 2001, **81**, 167.

25 Z. Zainal, L. K. Hui, M. Z. Hussein, A. H. Abdullah and I. R. Hamadneh, *J. Hazard. Mater.*, 2009, **164**, 138.

26 Q. Dai, L. Y. Shi, Y. G. Lu, J. L. Blin, D. J. Li and C. W. Yuan, *J. Photochem. Photobiol., A*, 2002, **148**, 295.

27 J. Xu, Y. Ao, D. Fu and C. Yuan, *Appl. Surf. Sci.*, 2008, **254**, 3033.

28 D. Li, H. Haneda, N. K. Labhsetwar, S. Hishita and N. Ohashi, *Chem. Phys. Lett.*, 2005, **401**, 579.

29 X. Cao, Z. Lu, L. Zhu, L. Yang, L. Gu, L. Caia and J. Chena, *Nanoscale*, 2014, **6**, 1434.

30 L. W. Zhu, L. K. Zhou, H. X. Li, H. F. Wang and J. P. Lang, *Mater. Lett.*, 2019, **95**, 13.